Modeling Tunnel Currents in Organic Permeable-Base Transistors[☆]

Akram Al-shadeedi^{c,1}, Shiyi Liu^c, Raj Kishen Radha Krishnan^c, Chang-Min Keum^{c,2}, Vikash Kaphle^c, Scott D. Bunge^d, Björn Lüssem^{c,*}

^aDepartment of Physics, Kent State University, Kent, OH, 44242, USA ^bDepartment of Chemistry and Biochemistry, Kent State University, Kent, OH, 44242, USA

Abstract

Research in Organic Permeable Base Transistors (OPBTs) has led to a significant increase in their performance. However, despite this progress, understanding of the working mechanism of OPBTs is still limited. Although first numerical models of OPBTs are able to describe the switching mechanism of OPBTs correctly, they neglect currents injected at the base electrode, which leads to unrealistically low off-currents and high ON/OFF ratios.

Here, a tunneling model is developed that is capable of describing injection of charges through a thin oxide layer formed around the base electrode of OPBTs. With the help of this injection model, the performance of the base-collector diode of OPBTs is discussed. In particular, the model is used to explain the reduction in backward currents due to an exposure to ambient air by an increase in the thickness of the oxide layer. Furthermore, the tunnel model is used to show that the reduction in backward currents of the base-collector diode leads to a decrease in off-currents of complete OPBTs, which in turn leads to an increase in their

[☆]Funding from the National Science Foundation (grant no. 1639073) and from the Bi-national Science Foundation (grant no. 2014396) is greatly acknowledged. Characterization of samples was partially done at the Characterization Facility of the Liquid Crystal Institute, Kent State University. CK and BL acknowledge funding from the Kent State University Internal Post-Doctoral Competition. AA was supported by The Higher Committee For Education Development in Iraq. We thank Tom Bangas (Kent State University) for testing and optimizing the tunnel injection model.

^{*}Corresponding author

Email address: blussem@kent.edu (Björn Lüssem)

¹Currently at: Department of Physics, University of Baghdad, Al-Jadriya, Baghdad, 10071, Iraq ²Currently at: Organic Semiconductor Centre SUPA, School of Physics and Astronomy, University of St Andrews, St Andrews KY16 9SS, UK

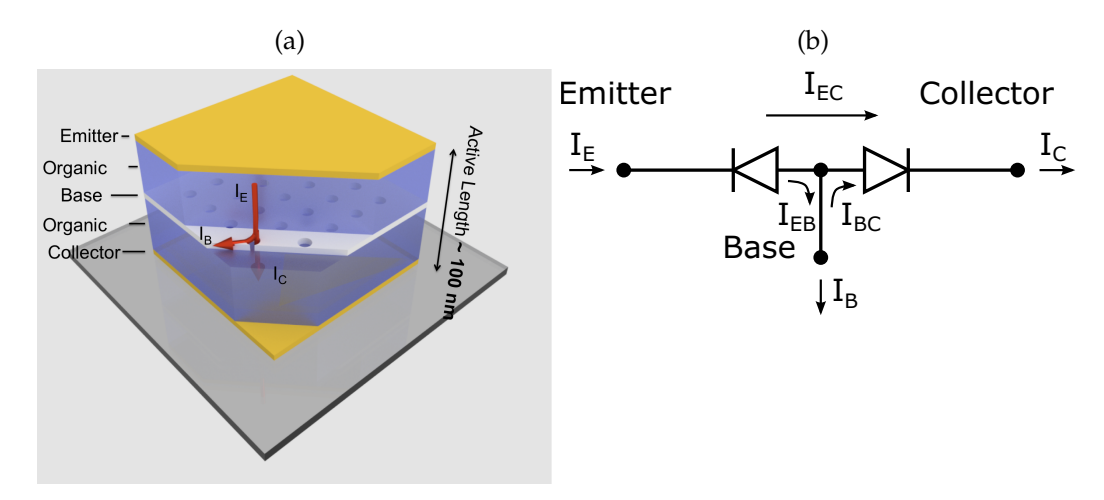


Figure 1: General structure of Organic Permeable-Base Transistors (OPBTs) (a). The devices consist of two Schottky diodes connected back-to-back - the upper one between the emitter and base electrode and the lower one between base and collector (b).

ON/OFF ratio.

Keywords: Organic Permeable-Base Transistors, Tunnel-Injection, Numeric Modeling

1. Introduction

Organic Permeable Base Transistors (OPBTs)¹ have made significant progress during the past years and nowadays reach a performance similar to more conventional OFETs.² OPBTs can drive very large currents (up to $1kA/cm^2$)³ at small voltages (1-2V),⁴ which results in high transconductance values,⁵ potentially leading to a significant increase in transit frequency into the 100MHz regime.^{3,6}

The structure of OPBTs is shown in Figure 1a. $^{2,5,7-9}$ OPBTs consist of two Schottky diodes that are connected back-to-back (cf. Figure 1b). Under normal operation, the top diode formed between emitter and base is operated in forward direction, i.e. the current injected at the emitter I_E is controlled by the voltage applied between emitter and base V_{BE} . The base, however, is very thin - in most reports, 10-15nm thick aluminum layers are used. 2,5,7,10 These thin layers are not closed but form small pinholes. 9 Hence, most of the current injected at the emitter I_E is transmitted through the base and is finally collected by the electric field of the reversely biased base-collector diode.

In best OPBTs, a transmission coefficient α defined as the ratio of the collector current to the emitter current ($\alpha \approx \frac{I_C}{I_E}$) above 99.99% is found.^{2,4} Furthermore, very large transconductance values are observed, which can sometimes reach up to several mS.^{3,4}

Unfortunately, despite these promising results, the practical use of OPBTs in larger integrated circuits is limited by significant base currents. Considering that the amplification of OPBTs, defined as the ratio of the collector current to the base currents ($\beta = \frac{I_C}{I_B}$), is currently in the range of 10^2 to 10^3 , 3,4 concatenating several OPBTs will lead to a large power dissipation.

Base currents can be reduced by exposing the devices to ambient air and annealing after processing the base electrode. 5,7 Yutani et al. argued that exposure to air partially oxidizes the Aluminum base electrode at the lower base $/C_{60}$ interface (i.e. the side of the base electrode facing the collector), which reduces the leakage current flowing from base to collector, 7 and therefore increases the ON/OFF ratio. Furthermore, Kaschura et al. showed that a native oxide layer on top of the base electrode (i.e. facing the emitter) is essential to effectively transport charge toward the pinholes in the base electrode, and to reach large driving currents. 11

Following these experimental results, all simulations used to model the operation of OPBTs add a thin Al_2O_3 layer around the base electrode. So far, this oxide layer is assumed to be ideal, i.e. leakage of tunnel currents through the base are not considered. This simplification of the device model is sufficient to discuss the fundamental switching mechanism of OPBTs, the fails to provide a better insight into the nature of base currents. In particular, neglecting base currents leads to a systematic overestimation of the ON/OFF switching ratio and the amplification of OPBTs.

In the following, this problem is addressed. A compact numerical model is presented to describe tunnel injection into organic semiconductors. The model is integrated into a drift-diffusion simulation to study the nature of the backward currents of base-collector diodes of OPBTs. The influence of exposure to air and subsequent annealing on the diode performance are studied experimentally and discussed with the help of the numerical model. Finally, the results obtained for the base-collector diode are used to explain the increase in the ON/OFF switching ratio of OPBTs observed when OPBTs are annealed in ambient air.

Overall, the numerical model combined with the experiments discussed here add to the current understanding of OPBTs and will help to develop a predictive device model of OPBTs capable of describing all aspects of device performance, including parameters that depend on the base currents such as the switching ratio

and the amplification.

2. Modeling Tunnel Injection Into Organic Semiconductors

Tunnel currents are an integral part of any charge transport model describing thermally activated hopping in disordered organic semiconductors. The hopping rate between adjacent states within the molecular layer can be described by Marcus theory, which predicts that the transfer rate is proportional to the electronic coupling between the initial and final hopping state.¹³

Often, in order to reduce the complexity of charge transport calculations, the electronic coupling between molecules is not explicitly determined. Instead, the transfer rate of electrons between adjacent molecules Γ_{MA} is approximated by the well known Miller-Abrahams transfer equation, which describes tunneling of charge carriers at thermally elevated energy levels. ¹⁴ The tunnel probability is approximated by an exponential factor $\exp(-2\gamma_0 R)$, with γ_0 the decay length or localization of the charge carrier on the molecule and R the distance between adjacent states $E_{initial}$ and E_{target} , which leads to

$$\Gamma_{MA} = \exp\left(-2\gamma_0 R\right) \begin{cases} \exp\left(-\frac{E_{target} - E_{initial}}{k_B T}\right) & \text{if } E_{target} > E_{initial} \\ 1 & \text{else} \end{cases}$$
 (1)

Based on the Miller-Abrahams rate, complex mobility models of organic semiconductors were developed that correctly describe the electric field and charge carrier dependence of the experimentally observed charge carrier mobility. 15,16 Overall, these models were very successful and were used to model charge transport in complex organic devices. 17,18

Arkhipov et al. ¹⁹ used a similar approach to model charge carrier injection from an electrode into an adjacent organic layer. Again, tunneling is described by an exponential tunnel term $\exp(-2\gamma_0x_0)$, where x_0 denotes the tunnel distance. Additionally, Arkhipov et al. account for the image charge of the injected charge carrier close to the metallic electrode, which leads to a reduction of the injection barrier Δ by $\frac{e^2}{16\pi\epsilon_0\epsilon x}$. Furthermore, the potential of the image charge alters the shape of the injection barrier and causes some of the injected charge carriers to return to the electrode after jumping into the semiconductor. Arkhipov et al. show that the well-known Onsager theory can be used to account for this back-drift/diffusion of charge carriers and include an escape probability w_{esc} to correctly describe the probability that the injected electron is able to overcome the attractive potential of the image charge. Overall, the injection current j_{inj}

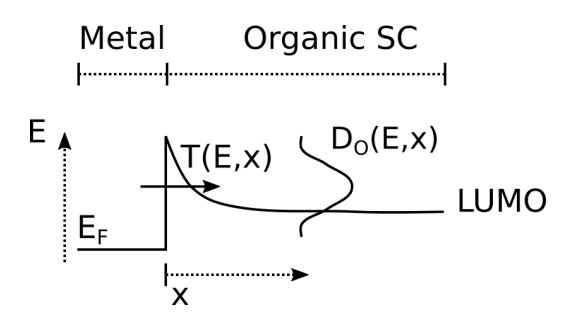


Figure 2: Tunnel injection model. The total electron injection rate at the cathode is calculated as the superposition of thermal injection (described by the thermodynamic equilibrium at the interface) and tunnel injection (described by the tunneling probability T(E) in Equation 5).

becomes 19

$$j_{inj} = ev_0 \int_a^\infty dx_0 \exp\left(-2\gamma_0 x_0\right) w_{esc}(x_0) \times \int_{-\infty}^\infty dE D_o\left(U_0(x_0) - E\right) \begin{cases} \exp\left(-\frac{E}{k_B T}\right) & \text{if } E > 0\\ 1 & \text{else} \end{cases}$$
(2)

with v_0 the attempt to jump frequency, a the first position inside the organic semiconductor, into which charge carriers can jump and $D_o(E)$ the gaussian density of state of an organic semiconductor. $U_0(x)$ is the electric potential inside the organic layer relative to the Fermi Level of the electrode, ¹⁹ including the potential of the image charge.

Although both approaches, i.e. the use of Equation 1 for charge transport calculations and 2 for calculation of injection currents, were highly successful, they neglect the energy dependence of the tunnel rate, i.e. the dependence of the decay length γ_0 on the energetic distance between the tunnel level and the injection barrier. This approximation is justified as the Miller-Abrahams is usually used to treat nearest neighbour hopping close to the transport level of the system. Due to the disordered nature of the organic semiconductor, an average tunnel barrier or decay length can be defined, that describes the macroscopic behavior of the system correctly.

However, to determine tunnel rates well below the transport level, i.e. at a very low density of states, the strong energy dependence of the decay length γ_0 has to be considered, in particular if charge carrier injection through a large injection barrier or even through a thin oxide layer formed at the metal/organic interface is studied.

The tunnel injection model is sketched in Fig. 2. The rate of electrons tunneling

into position x of the device $\Gamma(x)$ is calculated from 20,21

$$\Gamma(x) = \nu_0 \int_{-\infty}^{\infty} dE_m \int_{-\infty}^{\infty} dE_o D_o (E - \mu_o(x)) D_m (E - \mu_m) T(E_m, E_o) [f(E - \mu_m) - f(E - \mu_o(x))]$$

$$\approx \nu_0 \overline{D_m} \int_{-\infty}^{\infty} dE_m \int_{-\infty}^{\infty} dE_o D_o (E - \mu_o(x)) T(E_m, E_o) [f(E - \mu_m) - f(E - \mu_o(x))]$$
(3)

where μ_0 and μ_m are the electrochemical potentials inside the organic layer and metal, D_m is the density of states inside the aluminium electrode, f(E) is the Fermi-Dirac distribution, $T(E_m, E_o)$ is the tunneling probability from an initial state inside the metal electrode with energy E_m to a molecular state inside the organic layer at the energy E_o . In Equation 3, it is assumed the the density of states inside the metal varies much less compared to the density of states inside the organic layer, so that it can be treated as approximately constant. Assuming elastic tunneling, Equation 3 can be simplified further ($\Gamma_0 = \nu_0 \overline{D_m}$, $E_m = E_0 = E$, $\int_{E_m - \Delta_E/2}^{E_m + \Delta_E/2} dE_o D_o (E - \mu_o(x)) \approx D_o (E - \mu_o(x)) \Delta_E$, Δ_E : discretization of energy used in the simulation):

$$\Gamma(x) \approx \Gamma_0 \int_{-\infty}^{\infty} dE D_o \left(E - \mu_o(x) \right) \Delta_E T(E) \left[f(E - \mu_m) - f(E - \mu_o(x)) \right] \tag{4}$$

T(E) is estimated by

$$T(E,x) \approx \exp\left(-\frac{2}{\hbar} \int dx \alpha\right),$$
 (5)

with α describing the localization or decay of the wavefunction.

In order to calculate the decay of the wavefunction α , tunneling above and below the transport energy E_{tr} is calculated differently. Here, a definition of the transport energy given by Tietze et al. 22 is used, although other definitions can be included as well. 23 Tietze et al. showed that using the Boltzmann approximation, the density of free holes p inside a Gaussian Density of States $D_o(E) = \frac{N_0}{\sqrt{2\pi}\sigma} \exp\left(\frac{(E-E_0)^2}{2\sigma^2}\right)$ (N_0 : density of states, σ : width of the density of states, E_0 : maximum of the density of states) can be written as (equivalent for

electrons)

$$p = N_0 \exp\left(-\frac{E_{tr,0} - \mu_o}{k_B T}\right) \tag{6}$$

$$E_{tr,0} = E_0 + \frac{\sigma^2}{2k_BT}, \tag{7}$$

i.e. the transport energy $E_{tr,0}$ as defined by Equation 7 can be seen as equivalent to the valence band edge of inorganic semiconductors.

Equation 7 neglects the electric potential inside the organic layer and the effect of image charges close to the metal electrode. Therefore, it has to be adapted according to

$$E_{tr,x} = E_{tr,0} - e\phi(x) - \frac{e^2}{16\pi\epsilon\epsilon_0 x}$$
 (8)

where $\phi(x)$ is the electrostatic potential inside the organic layer as obtained by the drift-diffusion simulation and the third term in Eq. 8 represents the additional potential of the injected charge due to the electric field of the image charge (x: distance between the electrode and the charge).

Above the transport energy E_{tr} , $\alpha = \alpha_0$ is assumed as constant, effectively recovering Miller-Abrahams hopping rate. Below the transport energy, α is estimated by the Wentzel-Kramers-Brillouin (WKB) approximation

$$\alpha \approx \alpha_0 + \sqrt{(2m(E_{tr} - E))} \tag{9}$$

The electron tunneling rate as determined by Equations 4, 5, and 9 is included as electron generation rate into a numerical drift-diffusion solver, implemented following the description of Knapp and Ruhstaller et al.²⁴ However, according to the results of Arkhipov,¹⁹ not all electrons injected into the organic semiconductor are able to overcome the attractive potential of the image charge, but some of them migrate back into the electrode. To include this effect here, we only consider charges that experience an electric field that accelerates them away from the electrodes. This approach implicitly neglects diffusion of charge carriers back into the electrode, which is justified as the charge carrier density at the electrodes is small.

In addition to the injection rate, the organic semiconductor at the contact is assumed to be in thermodynamic equilibrium with the electrode, i.e. the charge concentration at the boundary between the organic layer and the electrode is approximated by Maxwell-Boltzmann statistics. In effect, injection at the blocking Aluminum contact is modeled by a combination of thermal injection (described by the steady-state charge carrier concentration at the boundary) and tunnel injection (described by the tunnel rate Γ).

Details of the model and parameters of all simulations shown in the remainder of the manuscript are given in the supplementary information. Furthermore, the operation of the numeric model is illustrated in the Supplementary Information (Figure S1 and S2) using a 50nm thick C_{60} layer contacted by an ohmic electrode at x=0nm and a tunnel contact at x=50nm (injection barrier of 0.4 eV) as example. To illustrate the importance of the energy dependence of the tunneling probability, the tunnel current is calculated for increasing disorder in the organic film, i.e. for an increasing width of the density of states σ . For the simulation parameters used in the Supplementary Information, a decrease in the width of the density of states leads to an increase in the injected currents. For a sharper density of states, more states are located close to the transport energy (cf. Equation 8), the probability to tunnel into these states is higher (cf. Equation 9), and the overall injection current increases.

3. Influence of Exposure to Ambient Air and Annealing on the Performance of C_{60} based Schottky Diodes

Before using the tunnel model to study the working mechanism of OPBTs, the nature of backward currents in the base-collector diode of OPBTs I_{BC} is studied experimentally. These backwards currents are a major contribution to the overall base currents and significantly diminish the ON/OFF ratio of OPBTs.

Schottky diodes shown in Figure 3 are prepared according to the procedures described in the experimental description. The devices consist of 100 nm Aluminum (Al) covered by 20 nm Chromium (Cr) as anode, a layer of intrinsic C_{60} as organic semiconductor, and a thin Al layer as cathode. As the cathode of the diode forms the base if used in a complete OPBT stack, the thickness of the cathode is varied from 13 nm to 19 nm, which, however, has no influence on current transport in the diodes (cf. Supplementary Information Figure S3). In order to ensure a reliable contact to the top electrode, the top contact is enhanced by 50 nm Al outside the active area. Similar to other reports on OPBTs, 2,4,5 the device is exposed to ambient air after deposition of the enhancement contact and annealed inside a nitrogen filled glovebox at a temperature of $60^{\circ}C$.

The influence of exposure on the I-V characteristics of the diode is shown in Figure 4a. Overall, the current drops by approximately one order of magnitude in

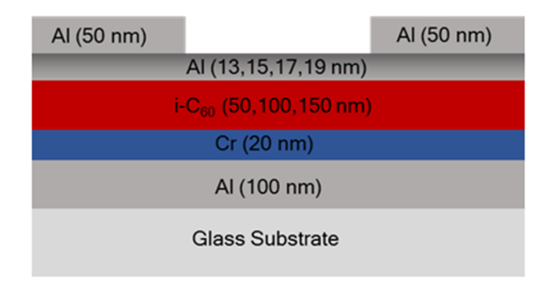


Figure 3: Structure of Organic Schottky Diodes (Base-Collector Diodes). The thickness of the C_{60} layer is varied (50, 100, and 150 nm).

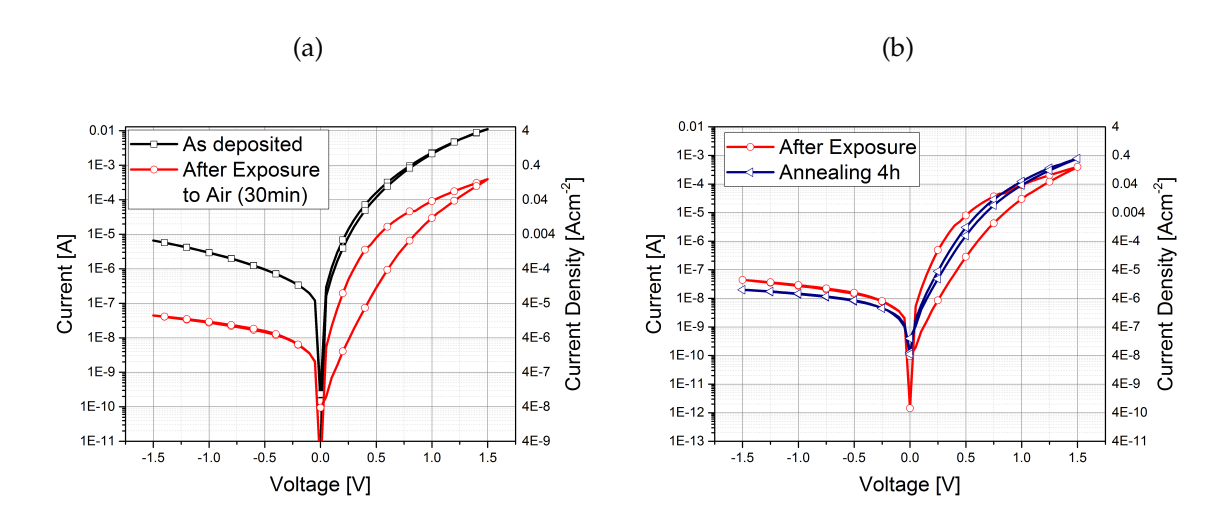


Figure 4: (a) Influence of air exposure on the bottom diode. Following 30 min of exposure to ambient air, the diode current decreases and a hysteresis in the characteristic becomes visible. However, as the off-current decreases faster than the on-current, the ON/OFF ratio of the diodes increases. (b) Influence of annealing in inert atmosphere at 60° C after exposure to ambient air on the electric characteristic of the diodes. The hysteresis shrinks with increasing of annealing time. Device Structure: 100 nm Al/10 nm Cr/100 nm $C_{60}/17$ nm Al, with active area 0.25 mm².

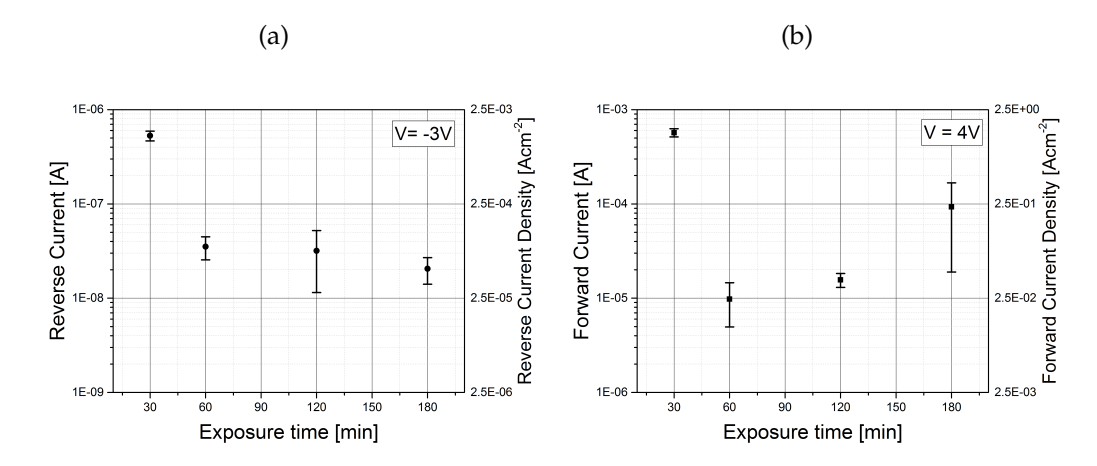


Figure 5: Influence of the duration the diodes are exposed to ambient air on the OFF current (a, measured at -3V) and ON current (b, measured at 4V). Device Structure for (a) and (b): 100 nm Al/20 nm Cr/100 nm $C_{60}/15$ -19 nm Al. The device area is $0.04mm^2$. Devices are annealed for 4h at 60° C.

forward direction after exposure to ambient air for 30 min, but by more than two orders of magnitude in reverse direction, overall increasing the ON/OFF ratio of the diodes. However, as Figure 4a shows as well, the increase in ON/OFF ratio is accompanied by an increase in the hysteresis of the measurement. The observation of an hysteresis in the electrical characteristic is in accordance with increased trap levels and reduced electron transport in C_{60} due to air exposure. ^{25,26}

Annealing at 60° C inside a nitrogen filled glovebox subsequent to air exposure leads to a reduction in the hysteresis of the diodes, which is shown in Figure 4b. It appears that the trap states inside the C_{60} -layer can partially be removed by an additional heating step in protective environment. Otherwise, the OFF-current remains constant for increasing annealing times and the ON-current increases slightly.

The reduction of forward and backward currents depends on the time the diodes are exposed to air. The backward current at -3V of a larger number of devices is shown in Figure 5a for varying exposure times (30 min to 180 min). The active area of the devices is 0.04 mm², the C_{60} layer is 100nm thick, and the top electrode has a thickness of 15 to 19 nm (i.e. realistic values used in the complete OPBT stack). After exposure to ambient air the devices are measured inside a glovebox filled with pure Nitrogen (oxygen and humidity levels below 0.1ppm).

Figure 5a exhibits that the backward current decreases further by almost one order of magnitude by increasing the exposure time from 30 min to 60 min. For

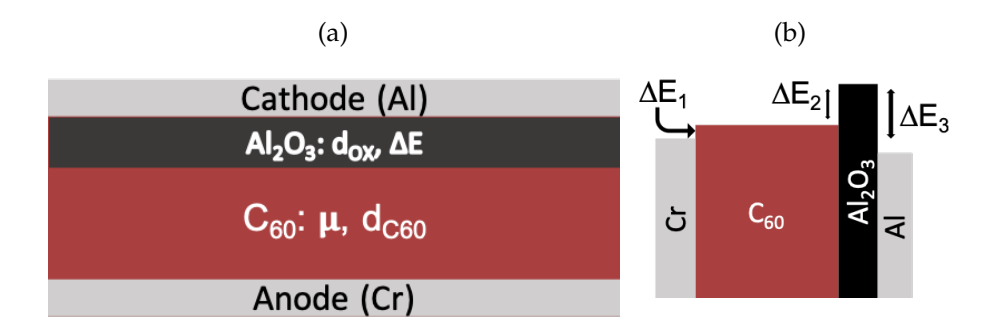


Figure 6: (a) Setup of the numerical model used to discuss the experimental results of Section 3. A thin oxide layer (injection barrier ΔE , thickness d_{OX} is included between the cathode and the organic semiconductor C_{60} (thickness d_{C60} , charge carrier mobility μ). (b) Definition of the energy barriers ΔE_1 , ΔE_2 , ΔE_3 at the Cr/C_{60} , C_{60}/Al_2O_3 and Al/Al_2O_3 interfaces. Details of the simulation parameters are given in the supplementary information.

longer times, the backward current starts to saturate (60 min to 180 min).

Unfortunately, as seen in Figure 4a, the reduction in reverse current is accompanied by a decrease of the forward current. In Figure 5b, the change in forward current is plotted vs. the exposure time. In contrast to the reverse current, the data is more scattered and no clear trend can be identified for exposure times ranging from 30 min to 180 min.

Overall, the Schottky diodes at the bottom of an OPBT can be optimized by exposure to ambient air. Both, the forward and backward currents decrease during the exposure step, but the decrease is stronger for the backward current, which is leading to an increase in the switching ratio of the diode. Furthermore, the hysteresis caused by air exposure can be partially reversed by an additional annealing step in protective environments without affecting the backward currents.

4. Modeling Optimized C_{60} Based Diodes and the Influence of Exposure to Ambient Air

To discuss the experimental results shown in the previous section (Section 3) with the help of the numerical model (Section 2) a structure as shown in Figure 6 is assumed. Following the results of Yutani et al.,⁷ a thin Al_2O_3 barrier layer is added between the C_{60} layer and the base electrode.

An optimized fit for the backward current of the diode with a 50nm thick C_{60} layer is shown in Figure 7a. A good agreement between the numerical model and the experimental result is obtained assuming an injection barrier between the

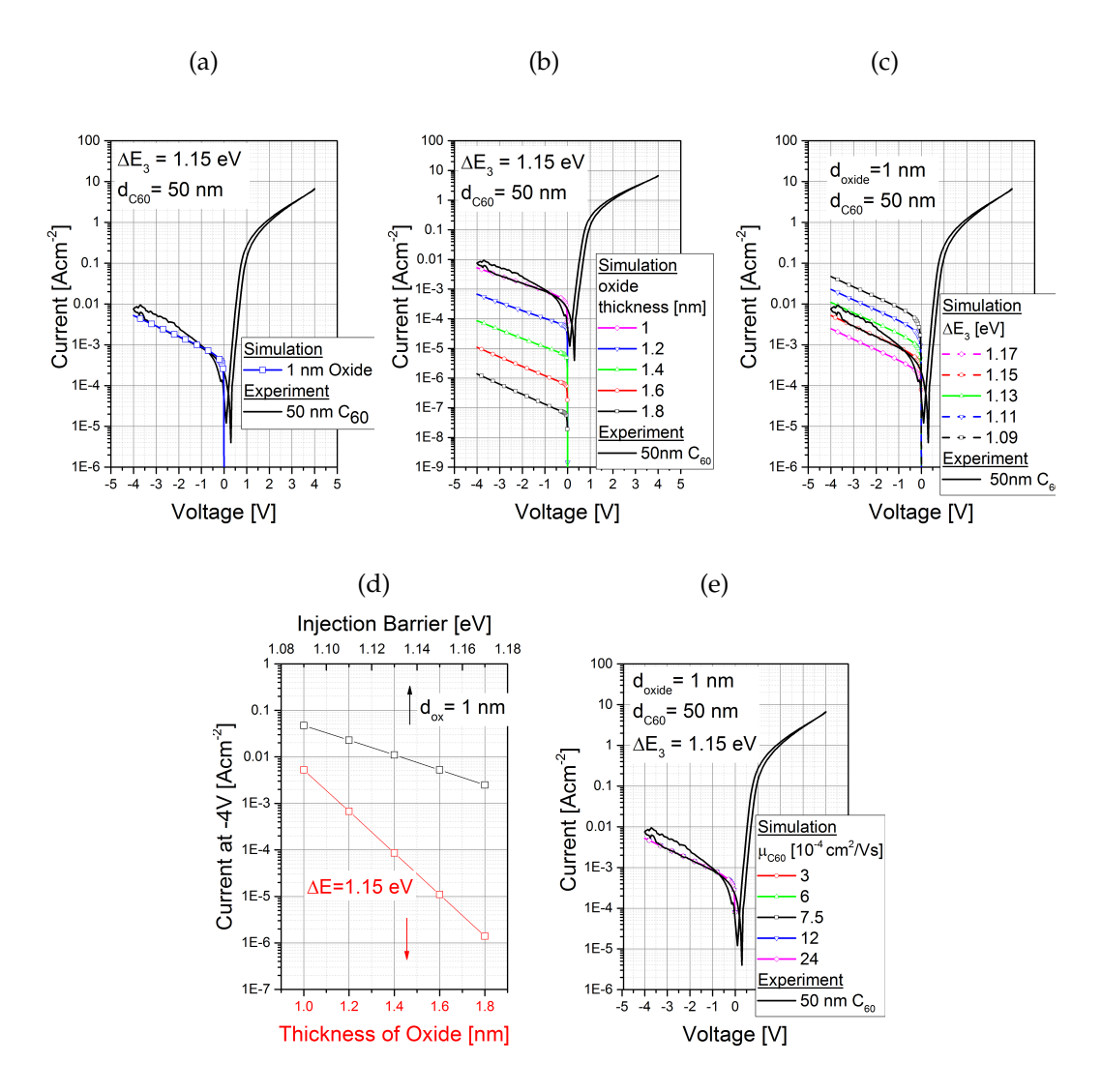


Figure 7: Influence of the C_{60} /Aluminium interface on the backward current observed in the diodes. The backward current can be modeled by assuming a thin oxide layer at the interface (a). The thickness of the oxide layer (b and d) and the tunnel barrier it presents (c and d) have a strong influence on the magnitude of the reverse current. The magnitude of the charge carrier mobility inside the organic layer does not influence the backward currents, reflecting the contact limitation of this device (e).

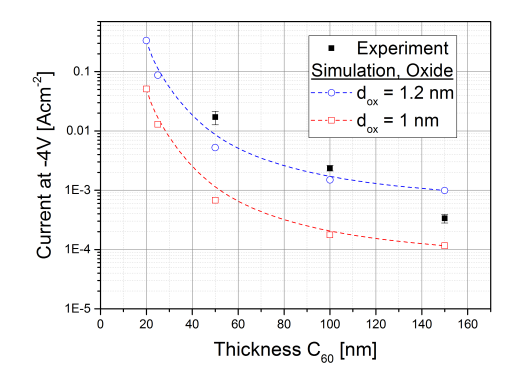


Figure 8: Dependence of the reverse current at V = -4V on the thickness of the C_{60} layer. Two series of calculations - one series assuming an Al_2O_3 layer of $d_{ox} = 1nm$ (blue) and another series with a slightly increased oxide layer thickness ($d_{ox} = 1.2nm$, red).

cathode and the thin Al_2O_3 layer of $\Delta E_3 = 1.15eV$ (cf. Figure 6b) and a thickness of the oxide layer of $d_{ox} = 1nm$. However, this result strongly dependents on the particular choice of model parameters. As seen in Figure 7b and 7c, the reverse current drops strongly for increasing thickness of the oxide layer (cf. Figure 7b) and for increasing height of tunnel barrier of the thin Al_2O_3 layer ΔE_3 (cf. Figure 7c). In fact, as shown in Figure 7d, these two parameters are correlated. This correlation is a direct consequence of the energy dependence of the transmission factor as defined in Section 2, i.e. the absolute value of the transmission can be decreased by both, an increase in the injection barrier and an increase in the thickness of the injection barrier.

The thickness of the tunnel barrier used here is below the thickness of $d \approx 3nm$ usually obtained for a native Al_2O_3 layer.²⁷ However, it has to be kept in mind that the tunnel barrier discussed here is not directly exposed to ambient conditions, but grows at the Al/C_{60} interface, i.e. at significantly different conditions. Furthermore, the tunnel barrier of thin Al_2O_3 is highly dependent on the growth conditions.²⁸ Overall, due to the correlation between simulation parameters and the corresponding uncertainty in their absolute values, only trends in the experimental data will be discussed in the following.

In contrast to the thickness of the oxide layer and the height of the injection barrier, the charge carrier mobility inside the C_{60} layer has no influence on the backward currents (cf. Figure 7e). This result shows that the current in backward direction is limited by the injection of electrons through the oxide layer, and that the injection rate is slower than the rate at which electrons are transported away

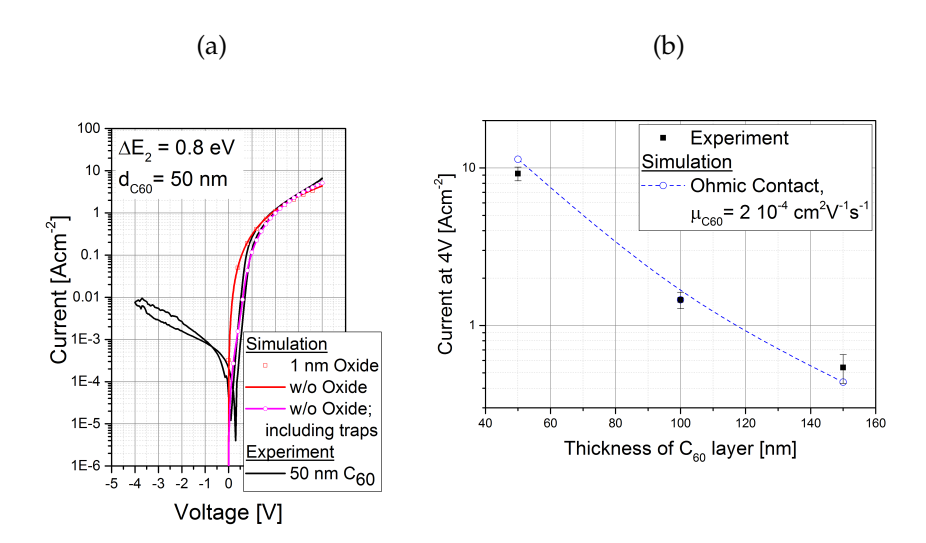


Figure 9: (a) Fitting the forward current with and without a thin oxide layer at the Aluminium/ C_{60} interface. (b) Thickness dependence of the experimental forward current. The devices show a $I \propto d^{-3}$ dependency, indicative of space charge limited currents.

from the electrode. Furthermore, the result indicates that the injection rate of electrons is too low to cause the formation of a significant space charge layer in reverse direction that could oppose the current flow.

In Figure 8 the influence of the current on the thickness of the C_{60} layer is plotted. The simulated current at -4V is plotted for two thicknesses of the oxide layer (1.2nm and 1nm) and compared to the experimental results. Both, simulation and experiment show an increase in current for thinner organic layers, which can be explained by a larger voltage drop across the oxide layer, leading to a higher electric field inside the oxide and hence a larger tunnel current.

The forward current fitted by the same model is shown by the red symbols in 9a assuming an barrier of $\Delta E_2 = 0.8eV$ (cf. Figure 6b) between the C_{60} layer and the oxide layer. This result is compared to the current obtained for a device without oxide layer, i.e. assuming a direct contact between the Aluminium electrode and the organic layer (red line). Both calculations lead to identical results, which shows the forward current is not limited by the thin oxide layer.

This observation is confirmed by the dependence of the forward current on the C_{60} layer thickness plotted in Figure 9. The experimental results show a dependency of $I \propto d^{-3}$. Additionally, the forward current scales with the square of the applied voltage (cf. Figure S₄ of the supplementary information), indicative of space charge limited currents. Space charge limited currents can only be

observed if the injection/extraction of charge carriers into or from the organic semiconductor is efficient, i.e. tunneling through the oxide layer is not limiting the forward currents. Indeed, the thickness dependency can be fitted by assuming a direct C_{60} /Aluminium contact (blue line in Figure 9) assuming a charge carrier mobility of C_{60} of $\mu = 2 \cdot 10^{-4} cm^2/Vs$.

The observation that the oxide layer is not limiting the current flow in forward direction can be explained by the asymmetry of the tunnel barrier for tunneling from the electrode (for currents flowing in backward direction, large barrier ΔE_3) compared to tunneling from the organic semiconductor (for currents flowing in forward direction, smaller barrier ΔE_2). Apart of the much lower tunnel barrier seen from the organic semiconductor, the high electric field inside the oxide will lead to a strong band bending and a reduction in the tunnel distance similar to Fowler-Nordheim injection model. Overall, this will lead to tunnel rates that are large enough to remove all electrons transported toward the thin oxide layer, i.e. the oxide layer does not suppress the current in forward direction.

The absolute value of the mobility of the C_{60} film deduced from Figure 9 is much lower than mobilities reported for organic field-effect transistors. This low mobility can be correlated to the reduction in forward current of the diode after exposure to ambient air (cf. Figure 4a). Furthermore, the increase in trap levels as indicated by the observed hysteresis after exposure to air and additional degradation of the C_{60} film can explain this low mobility. In fact, fitting of the forward current can be improved for low voltages (i.e. below 1V), if trap states are added into a thin layer (2nm, density of traps $N_{trap} = 5 \cdot 10^{-19} cm^{-3}$) adjacent to the Aluminium electrode (Figure 9a, pink line).

Following the above results, the decrease in reverse current with increasing exposure time observed in Figure 5a can be explained by an increase in the thickness of the oxide layer with increased exposure time. In Figure 10, the reverse current at -3V is plotted vs. the thickness of the oxide layer d_{ox} as obtained by the numerical model (thickness of C_{60} layer is 100 nm). Using Figure 10 the effective oxide thickness for different exposure times are 0.98 nm (30 min), 1.2 nm (for 60 min and 120 min) and 1.3 nm (180 min). However, considering the correlation between the injection barrier and thickness of the oxide layer shown in Figure 7d, only the trend in the data should be considered and not absolute thickness values.

5. Influence of Exposure to Ambient Air on the ON/OFF ratio of Organic Permeable Base Transistors (OPBTs)

The tunnel model as discussed above can be used to discuss the operation of OPBTs and to devise ways to improve their performance. Some OPBTs, in

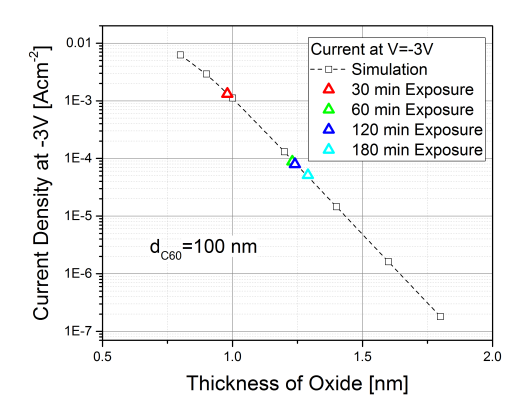


Figure 10: Dependence of the simulated reverse current at V = -3V on the thickness of the tunnel oxide layer (thickness of C_{60} layer is 100 nm). The decrease in reverse current as shown in the experimental section (Figure 5a, experimental results plotted by solid symbols) can be explained by a slight growth in the thickness of the tunnel oxide layer (from approx. 1nm to 1.3nm).

particular OPBTs with large device areas, show large off state currents and therefore a moderate ON/OFF switching ratio only. In the off-state of OPBTs, a large voltage is applied between the base electrode and the collector electrode. Therefore, the backward current of the diode between these two electrodes - the base and collector - is a major contribution to the OFF-currents of an OPBT (cf. Figure 1b), i.e. the ON/OFF ratio of OPBTs can be increased by an optimization of the bottom Schottky diode and a reduction of its backward currents. Following the results discussed above, this can be done by an increase in the thickness of the organic layer (cf. Figure 8), an increase of the time the cathode is exposed to ambient air (cf. Figure 5), and additional thermal annealing (cf. Figure 4b).

The details of the OPBT structure discussed here are shown in Figure 11. The lower part of the device (Glass substrate/Al/Cr/ C_{60} /Al) is identical to the Schottky diodes discussed above, i.e. all results gathered above can be used to discuss the OPBT performance. The upper part (Al/ C_{60} /n-doped C_{60} /Cr/Al) represents the top diode. The top electrode is used as emitter, the middle electrode as base, and the lower electrode as collector.

Figure 12 shows the transfer characteristic of this OPBT. The sample is annealed in two steps: firstly, devices are annealed for 2h at a temperature of $150^{\circ}C$ inside the glovebox, followed by a second annealing step outside the glovebox for 2h at a temperature of $120^{\circ}C$.

Figure 12 displays the collector current of OPBTs with and without annealing

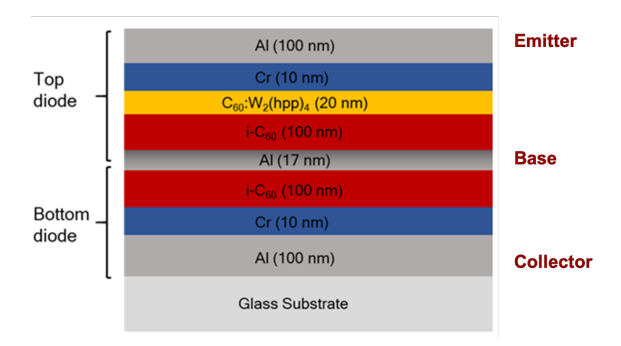


Figure 11: Structure of a C_{60} based OPBT with 17 nm base electrode thickness and active area 4 mm².

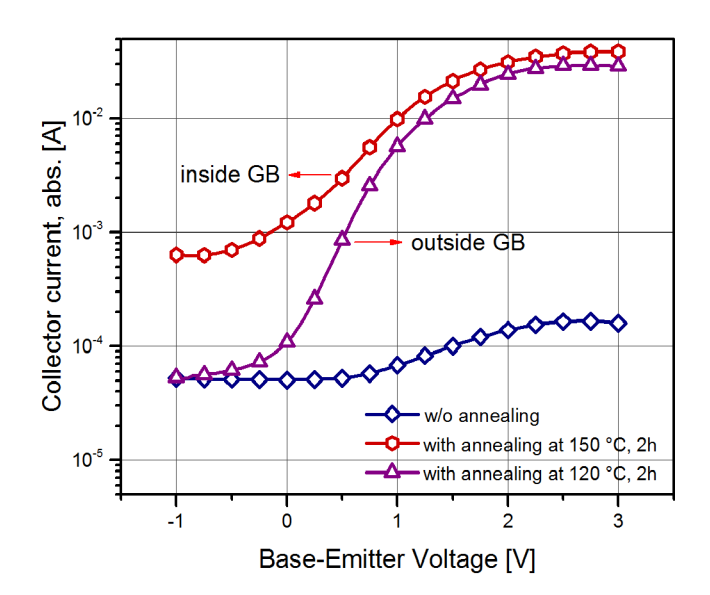


Figure 12: Collector current versus base-emitter voltage at V_{CE} = 3 V before annealing (blue), after annealing inside a nitrogen filled glovebox (red) at $150^{\circ}C$, and after additional annealing in ambient air (purple) at $120^{\circ}C$. Active overlap area is 4 mm².

versus the base-emitter voltage at a constant voltage between collector and emitter of V_{CE} = 3 V. Samples without annealing exhibit almost no transistor behavior and the collector currents increase weakly with base-emitter voltage in the range from 1 V to 3 V. Overall, the ON/OFF ratio is small and reaches 3 only.

After annealing inside the glovebox, the collector current increases and the ON-state currents (at V_{BE} = 3 V) can be clearly distinguished from the OFF-state currents (V_{BE} = -1 V). Overall, the ON-state currents increase by two orders of magnitude.

This effect of increasing transmission after annealing was already described by Fischer et al.⁵ They explained this apparent increase in the ON-state current by a re-organization inside the C_{60} layer, which stresses the thin aluminum base electrode and increases the density of holes or pores in the base. Due to the increased density of openings in the base electrodes, the transmitted current I_{EC} increases, leading to an increase in collector current I_C in the on state.

However, annealing devices inside the glovebox increases both the ON-state and OFF-state currents, indicating that not only the transmitted current I_{EC} increases, but as well the leakage current I_{BC} . Overall, annealing inside the glovebox leads to an ON/OFF ratio of below 100.

Following the results of Section 3, an additional exposure of devices to ambient air or even annealing devices outside the glovebox has the potential to decrease I_{BC} and to lead to a better performance.

Indeed, as shown in Figure 12 the ON-state of the device annealed in ambient air is almost identical to the ON-state of samples annealed inside the glovebox, but the OFF-state currents are significantly reduced, which results in an increase in the ON/OFF ratio to almost 10^3 .

This reduction in the OFF-state current is in line with the results of the Schottky diodes described above and can be explained by a reduction in backward current of the bottom diode, most pronounced if the potential difference between the emitter and base V_{BE} is zero or negative and the potential between collector and base V_{CE} is large.

To discuss this reduction in the OFF-state currents in more detail, a full transfer characteristic of an OPBT annealed in ambient air is shown in Figure 13a. The device shows a high performance, i.e. a high transmission of above 99.9% at 1V and a high amplification of 2 to 3 orders of magnitude. Overall, the transconductance of the devices is large and exceeds 20 mS (Figure 13b), which shows the potential for large switching frequencies of this device.

In Figure 13a the results of a series of simulations calculating the backward currents for different thickness of the oxide layer are shown and compared to

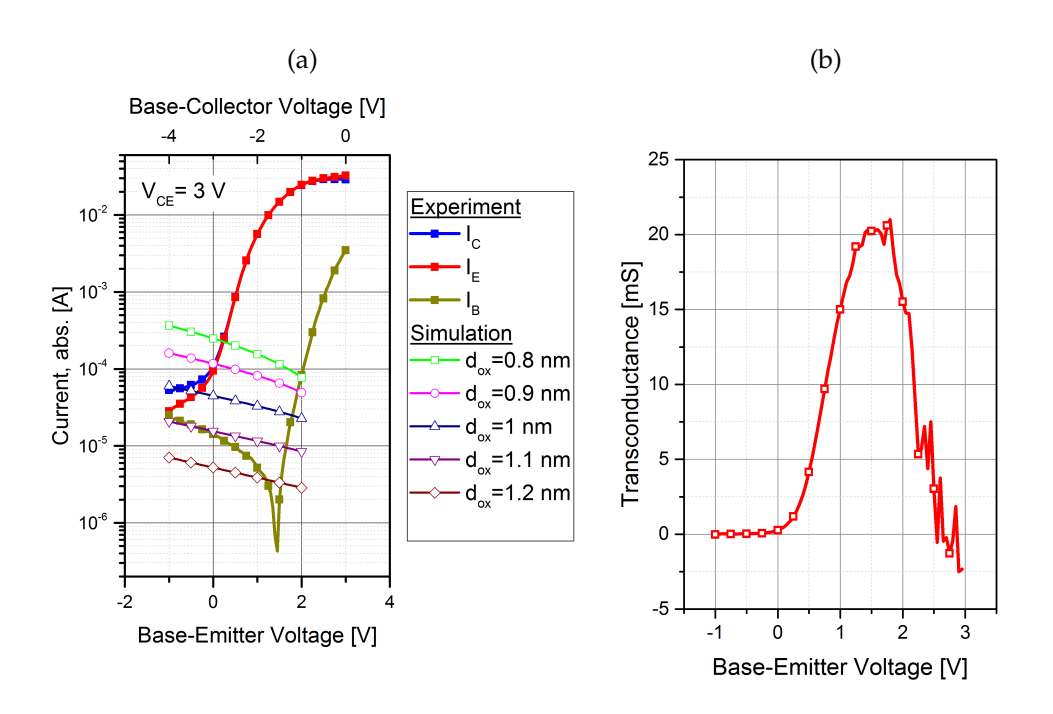


Figure 13: (a) Transfer characteristic of OPBT annealed at $120^{\circ}C$ in ambient air (Driving Voltage V_{CE} = 3 V, device area: $4mm^2$, device structure 100 nm Al, 10 nm Cr, 100 nm intrinsic C_{60} , 13 nm Al, 100nm intrinsic C_{60} , 20 nm n-doped C_{60} , 10 nm Cr, 100 nm Al). Included in part (a) is the IV characteristic of the simulated bottom diode with increasing thickness of the oxide layer at the Al/ C_{60} interface. (b) Transconductance of the OPBT shown in (a) reaching a maximum of 20mS.

the transfer characteristic. The top x-axis represents the voltage that is applied between the base and collector, keeping the potential between collector and emitter V_{CE} constant at 3V. As can be seen in the figure, the backward current of the simulated diodes matches the off current of the OPBT if one assumes a thickness of the oxide layer of $d_{ox} = 1nm$. Furthermore, the reduction in the OFF state current can be explained by an increase in the oxide thickness from approx. $d_{ox} = 0.8nm$ to 1nm.

6. Conclusion

Organic Permeable Base Transistors (OPBTs) show a very high performance and are candidates for future flexible electronic circuits. However, a further improvement of OPBTs is currently hampered by a limited understanding of the working mechanism of these transistors. In particular, all models describing the device operation proposed so far cannot describe the origin and magnitude of base currents in these devices, which in turns makes it impossible to predict the ON/OFF ratio of OPBTs and their amplification.

Here, base currents in OPBTs are treated as tunnel currents through a thin oxide layer surrounding the base electrode, which is formed during an intentional exposure step of the device to ambient air. A numerical drift-diffusion model is presented that is capable of describing these tunnel currents. The energy dependence of the tunnel injection probability at the base electrode is calculated by a slightly adapted WKB tunneling expression and included into the drift-diffusion model as an electron generation rate.

Experimentally, the influence of air exposure and annealing on OPBTs and in particular the base-emitter diode of OPBTs is studied. It is shown that an extended exposure of the individual diodes to ambient air leads to a reduction in the backward current. With the help of the simulation, the decrease in the backward current can be explained by a slight increase in oxide layer thickness at the base/ C_{60} interface. Furthermore, it is shown that in forward direction, the devices are not limited by the oxide layer, i.e. tunneling in forward direction through this layer is very efficient. Instead, the current in forward direction is limited by space charge limited currents and show the expected $I \propto V^2/d^3$ dependency.

The experimental and simulation results obtained from the Schottky diodes can be applied to optimize full OPBTs. It is shown that and additional exposure of complete OPBT to ambient air and subsequent annealing leads to a reduction in OFF state current of these transistors with only a minor reduction in the ON

current. Again, this behavior is explained by an increase in the thickness of the oxide layer surrounding the base electrode and consequently a reduction in the backward current of the bottom diode of the OPBT.

The numerical model of the tunnel currents described here provides for a framework to discuss trends in organic Schottky diodes and OPBTs. However, it has to be kept in mind that correlations exist between the simulation parameters in particular between the injection barrier at the base electrode ΔE_3 and the thickness of the oxide layer d_{ox} . Therefore, the focus of this study is on explaining trends observed in the experiments rather then extract quantitative device parameters.

Overall, the results described here add to the understanding of OPBTs. The proposed one-dimensional model of the Schottky diodes, which represents the fundamental building blocks of the OPBTs, is a first step toward an experimentally verified full (two dimensional) model of OPBTs. In particular, the inclusion of tunnel injection currents at the base electrode will lead to a more thorough understanding of the nature of base currents, which at the current state of OPBT performance limit the use of these devices in larger integrated circuits.

7. Experimental Details

Diodes and organic permeable-base transistors (OPBTs) are prepared by thermal evaporation in a custom built system (EvoVac, Angstrom Engineering) with a background pressure below 10⁻⁷ mbar. The devices are structured by shadow masks.

All devices are fabricated on glass substrates. Glass substrates are cleaned in subsequent ultrasonic baths of soap and DI water, DI water, Acetone, Methanol, and Isopropyl alcohol. Afterwards, the substrates are dried by Nitrogen gas.

The structure of the bottom diode is shown in Figure 3. The devices consist of 100 nm Aluminium (Al) covered by 10-20 nm Chromium (Cr) as anode, a layer of intrinsic C_{60} as organic semiconductor, and a thin Al layer as a cathode. Outside the device area, the cathode is enhanced by a 50 nm Al contact pad, which does not contribute to the active area. After depositing the enhancement contact, the device is exposed to ambient air as described in the main text.

The active area of the diode sketched in Figure 3 is defined by the overlap of the anode and cathode, yielding a device area of 4 mm². The results displayed in Figure 5 a and b are obtained for a smaller device area (0.04 mm²), which was obtained using a bank structure of 100nm of SiOx, similar to the structure described by Klinger et al.⁴

Figure 1 shows the structure of the OPBT. The top and bottom electrode consist of a combination of Al (100 nm) and Cr (20 nm). Using of chromium layer ensures

a sufficient electron injection into C_{60} . A thin Al layer with a thickness of 17nm is used as the base electrode (which represents the cathode layer in bottom and top diode) and is exposed to ambient air for 30 min. The top 20 nm thick C_{60} layer is doped with a highly efficient n-dopant $(W_2(hpp)_4)$ to improve the electron injection by reducing the contact resistance. ²⁹ Doping of C_{60} is accomplished by co-evaporating C_{60} and $W_2(hpp)_4$ at a concentration of 2 wt%.

Aluminum is purchased from Sigma-Aldrich with a purity of 99.999% and chromium is purchased from Angstrom Engineering Inc. with a purity 99.9%. C_{60} is purchased from Creaphys with a purity of 99.99%. The n-dopant $W_2(hpp)_4$ is synthesized and the method is demonstrated in Ref.³⁰ All samples are electrically characterized by a semiconductor parameter analyzer (4200-SCS,Keithley) inside the glovebox.

The numerical model is implemented in MATLAB. To enable a dense discretization in position (Δ_x) and energy (Δ_E), the tunnel rate is calculated on a highly parallel GPU unit (NVIDIA Tesla V100). To further increase the speed of the model, the tunneling distance is limited to 20nm; otherwise the tunneling rate is assumed to have dropped to negligible values.

Most of the results are obtained from a steady-state solution, i.e. setting all time derivatives to zero. However, for large tunnel rates, the steady-state calculations show poor convergence. Therefore, for the forward current calculation shown in Figure 9aa, red line a transient simulation with small time increments is used.

- [1] Yang, Y.; Heeger, A. J. Nature 1994, 372, 344–346.
- [2] Lüssem, B.; Günther, A.; Fischer, A.; Kasemann, D.; Leo, K. *Journal of Physics: Condensed Matter* **2015**, 27, 443003.
- [3] Klinger, M. P.; Fischer, A.; Kaschura, F.; Widmer, J.; Kheradmand-Boroujeni, B.; Ellinger, F.; Leo, K. *Scientific Reports* **2017**, 7.
- [4] Klinger, M. P.; Fischer, A.; Kaschura, F.; Scholz, R.; Lüssem, B.; Kheradmand-Boroujeni, B.; Ellinger, F.; Kasemann, D.; Leo, K. *Advanced Materials* **2015**, 27, 7734–7739.
- [5] Fischer, A.; Scholz, R.; Leo, K.; Lüssem, B. Applied Physics Letters 2012, 101, 213303.
- [6] Chen, W.; So, F.; Guo, J. Journal of Applied Physics 2014, 116, 044505.
- [7] Yutani, K.; Fujimoto, S.-y.; Nakayama, K.-i.; Yokoyama, M. *Molecular Crystals and Liquid Crystals* **2006**, 462, 51–57.

- [8] Nakayama, K.-i.; Fujimoto, S.-y.; Yokoyama, M. *Organic Electronics* **2009**, *10*, 543–546.
- [9] Yu, H.; Kim, J. H.; Chen, W.; Kim, D.; Guo, J.; So, F. Advanced Functional Materials 2014, 24, 6056–6065.
- [10] Fischer, A.; Siebeneicher, P.; Kleemann, H.; Leo, K.; Lüssem, B. *Journal of Applied Physics* **2012**, 111, 044507.
- [11] Kaschura, F.; Fischer, A.; Klinger, M. P.; Doan, D. H.; Koprucki, T.; Glitzky, A.; Kasemann, D.; Widmer, J.; Leo, K. *Journal of Applied Physics* **2016**, 120, 094501.
- [12] Luessem, B.; Tietze, M. L.; Fischer, A.; Pahner, P.; Kleemann, H.; Guenther, A.; Kasemann, D.; Leo, K. *Proceedings of SPIE* **2014**, *9185*, Conference on Organic Field-Effect Transistors XIII and Organic Semiconductors in Sensors and Bioelectronics VII, San Diego, CA, AUG 18-20, 2014.
- [13] Coropceanu, V.; Cornil, J.; da Silva Filho, D. A.; Olivier, Y.; Silbey, R.; Brédas, J.-L. *Chemical Reviews* **2007**, *107*, 926–952.
- [14] Schmechel, R. Physical Review B 2002, 66, 235206.
- [15] Bässler, H. physica status solidi (b) **1993**, 175, 15–56.
- [16] Bouhassoune, M.; van Mensfoort, S. L. M.; Bobbert, P. A.; Coehoorn, R. *Organic Electronics* **2009**, *10*, 437–445.
- [17] Mesta, M.; Carvelli, M.; de Vries, R. J.; van Eersel, H.; van der Holst, J. J. M.; Schober, M.; Furno, M.; Lüssem, B.; Leo, K.; Loebl, P.; Coehoorn, R.; Bobbert, P. A. *Nature Materials* **2013**, *12*, 652–8.
- [18] Schober, M.; Anderson, M.; Thomschke, M.; Widmer, J.; Furno, M.; Scholz, R.; Lüssem, B.; Leo, K. *Physical Review B* **2011**, *84*, 165326.
- [19] Arkhipov, V. I.; Emelianova, E. V.; Tak, Y. H.; Bassler, H. *Journal of Applied Physics* **1998**, *84*, 848–856.
- [20] Ferry, D. K.; Goodnick, S. M. *Transport in nanostructures*; Cambridge University Press, 1997.
- [21] Delerue, C.; Lannoo, M. *Nanostructures: Theory and Modelling*; Nanoscience and Technology; Springer Verlag, 2004.

- [22] Tietze, M. L.; Burtone, L.; Riede, M.; Lüssem, B.; Leo, K. *Physical Review B* **2012**, *86*, 035320.
- [23] Arkhipov, V.; Emelianova, E.; Adriaenssens, G. *Physical Review B* **2001**, *64*, 125125.
- [24] Knapp, E.; Häusermann, R.; Schwarzenbach, H.; Ruhstaller, B. *Journal of Applied Physics* **2010**, *108*, 054504.
- [25] Ahmed, R.; Simbrunner, C.; Schwabegger, G.; Baig, M.; Sitter, H. *Synthetic Metals* **2014**, *188*, 136 139.
- [26] Tapponnier, A.; Biaggio, I.; Günter, P. Applied Physics Letters 2005, 86, 2114.
- [27] Evertsson, J. et al. *Applied Surface Science* **2015**, 349, 826–832.
- [28] Wilt, J.; Gong, Y.; Gong, M.; Su, F.; Xu, H.; Sakidja, R.; Elliot, A.; Lu, R.; Zhao, S.; Han, S.; Wu, J. Z. *Physical Review Applied* **2017**, 7.
- [29] Menke, T.; Ray, D.; Meiss, J.; Leo, K.; Riede, M. *Applied Physics Letters* **2012**, 100, 093304.
- [30] Al-Shadeedi, A.; Liu, S.; Keum, C.-M.; Kasemann, D.; Hoßbach, C.; Bartha, J.; Bunge, S. D.; Lüssem, B. *ACS Applied Materials & Interfaces* **2016**, *8*, 32432–32439.
- [31] Selberherr, S. *Analysis and simulation of semiconductor devices*; Springer Science & Business Media, 2012.
- [32] Coehoorn, R.; Pasveer, W.; Bobbert, P.; Michels, M. *Physical Review B* 2005, 72, 155206.

Supplementary Information: Modeling Tunnel Currents in Organic Permeable-Base Transistors

Akram Al-shadeedi^{c,1}, Shiyi Liu^c, Raj Kishen Radha Krishnan^c, Chang-Min Keum^{c,2}, Vikash Kaphle^c, Scott D. Bunge^d, Björn Lüssem^{c,*}

^cDepartment of Physics, Kent State University, Kent, OH, 44242, USA ^dDepartment of Chemistry and Biochemistry, Kent State University, Kent, OH, 44242, USA

1. Details of the Drift-Diffusion Model

In the numerical model²⁴ used to discuss the electric characteristics of the Schottky diodes, Poisson's equation in 1D

$$\frac{d}{dx}\epsilon \frac{d}{dx}\Phi = q(n+n_t) \tag{S1}$$

 $(Φ: electric potential, q: elementary charge, n: electron density, <math>n_t$: density of trapped electrons) and the charge continuity equation

$$\frac{d}{dx}j_n = q(R - G) \tag{S2}$$

(j_n : electron current, R: recombination rate, G: generation rate) are solved numerically.

Email address: blussem@kent.edu (Björn Lüssem)

[☆]Funding from the National Science Foundation (grant no. 1639073) and from the Bi-national Science Foundation (grant no. 2014396) is greatly acknowledged. Characterization of samples was partially done at the Characterization Facility of the Liquid Crystal Institute, Kent State University. CK and BL acknowledge funding from the Kent State University Internal Post-Doctoral Competition. AA was supported by The Higher Committee For Education Development in Iraq. We thank Tom Bangas (Kent State University) for testing and optimizing the tunnel injection model.

^{*}Corresponding author

¹Currently at: Department of Physics, University of Baghdad, Al-Jadriya, Baghdad, 10071, Iraq

²Currently at: Organic Semiconductor Centre SUPA, School of Physics and Astronomy, University of St Andrews, St Andrews KY16 9SS, UK

The Gummel algorithm is used to ensure consistency between the solution of Equations S1 and S2, i.e. the two equations are subsequently solved until convergence is reached.

The Scharfetter-Gummel discretization scheme is used for Equation S2, and Boltzman statistics³¹ is implicitly assumed. A stabilized version of Equation S1 is used²⁴

$$\frac{d}{dx}\epsilon/q\frac{d}{dx}\Phi^{k+1} - \left[\frac{n^k + p^k}{U_t}\left(\Phi^{k+1} - \Phi^k\right)\right] = (n^k + n_t^k) \tag{S3}$$

where the superscript k indicates the kth iteration of the Gummel algorithm. As can be seen, Equation S₃ is identical to Equation S₁ in case of convergence, but Equation S₃ leads to a more stable performance of the algorithm.

Thermal injection at the electrode is treated by assuming thermal equilibrium between the metal and the organic semiconductors, i.e. the boundary condition at the contact (but inside the organic semiconductor) is chosen according to Boltzmann statistics. In case of tunnel injection, the tunnel rate calculated by Equation 5 of the main manuscript is included as generation rate *G* into equation S2.

For the simulations shown here, a constant charge carrier mobility is used as the emphasis of the manuscript is on explaining the trends observed in the experiment and not on providing a predictive numerical model. However, a charge carrier and electric field dependent mobility can be included as well,³² which has to be complemented with a Gaussian Density of states inside the organic semiconductor and the generalized Einstein equation.²⁴

2. Details of the Tunnel Model

The operation of the tunnel injection model described in the main text is illustrated in Figure S1 using a 50nm thick C_{60} layer contacted by an ohmic electrode at x = 0nm and a tunnel contact at x = 50nm (injection barrier of 0.4 eV) as test case (Figure S1).

The energy levels as obtained from the drift-diffusion simulation are shown in Figure S1a. The levels shown here correspond to the transport level as defined in Equation 9 of the main manuscript for holes (refereed to as HOMO) or an equivalent definition for the transport level of electrons (referred to as LUMO). At the right contact, the attractive potential of the image potential experienced by injected electrons is added to the transport level of the electrons to illustrate the energy landscape seen by an electron tunneling through the injection barrier.

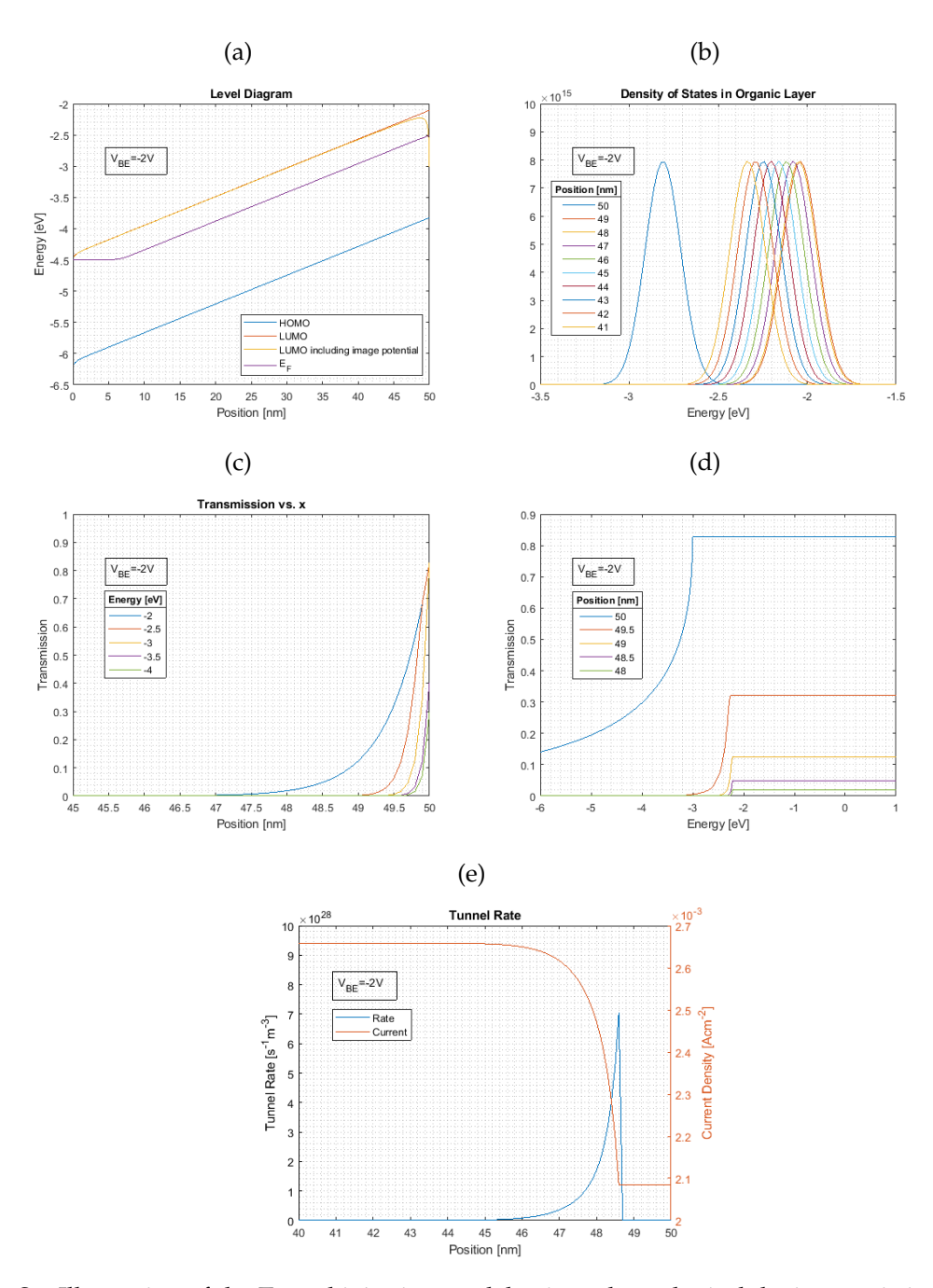


Figure S1: Illustration of the Tunnel injection model using a hypothetical device consisting of an ohmic electrode, a 50nm thick C_{60} layer, and a blocking electrode on the right (injection barrier $\Delta E = 0.4eV$. Details of the device parameter are given in the supplementary information. Part (a) shows the level diagram of the device at V = -2V. To calculate the injection rate, the LUMO energy is corrected by the image potential close to the right electrode. Part (b) plots the Gaussian Distribution of States at different positions inside the organic layer (normalized by the energy and space resolution, i.e. $\Delta_E \Delta X D_O$ is plotted), (c) the transmission probability T(E,x) as a function of the position inside the device as calculated by Equations 6 and 10, (d) the same transmission probability but as a function of energy. Finally, the tunnel rate as calculated by Equation 5 is shown in part (e). Due to the injection of electrons, the current density inside the organic layer increases continuously until it saturates at about 6nm away from the injecting electrode.

The level diagram in Figure S1a shows an almost constant slope of the transport levels at an applied voltage of -2V, i.e. an approximately constant field, which indicates that the injection of charge carriers is too weak to reach a space charge limited regime. Corresponding with the level diagram, the Gaussian density of electron transport states $D_o(x)$ shifts strongly closest to the electrode (due to the image potential), but shifts linear with distance to the electrode for larger distances (cf. Figure S1b). With the help of the density of states, the transmission T(E,x)can be calculated according to Equation 6, which leads to an exponential decay of the transmission into the organic layer (cf. Figure S1c). The energy dependence of the transmission coefficient T(E,x) is shown in Figure S1d. As discussed above, the transmission coefficient is calculated differently for two regimes: for tunneling above or at the transport level, the decay length γ_0 is assumed to be independent on the energy, which resembles conventional transport calculations using a Miller-Abrahms form of the hopping rate. Below the transport energy, however, the energy dependency of the decay length is included in the calculation (Equation 10), which leads to a strong dependency of the tunnel probability.

Finally, S1e plots the resulting injection rate, which is added to the continuity equation of the drift-diffusion calculation. To account for injected charges that drift back into the right electrode due to the attractive potential of the image charge, only charges injected into a region with an electric field pointing away from the electrode are accounted for. The injected electrons add to the current density, which is shown in S1e as well. Finally, far away from the electrode, the injection rate drops to negligible values and the current density remains constant.

Figure S1d already shows that the energy dependence of the tunnel injection current is significant. This dependency has some important consequences for the qualitative understanding of injection into organic semiconductors.

In Figure S2 the dependency of the tunnel injection current on the width of the Gaussian density of states σ is plotted. The relative strength of two opposite trends are expected to determine the overall dependency of the injected current on σ . On the one hand, a broader density of states leads to a larger number of states close to the Fermi-Level of the injecting contact, i.e. electrons have to tunnel a shorter distance into the organic layer even at low applied voltages. On the other hand, a broader density of states leads to a lower number of states close to the transport level (assuming that the total number of states remains constant), i.e. at energy levels that show a higher transmission probability T(E,x).

Overall, the model presented here predicts a decrease of the tunnel rate (cf. Figure S2a) and the injected current (cf. Figure S2a) for increasing σ . The influence of a higher transmission probability at higher energies outweighs an increase of

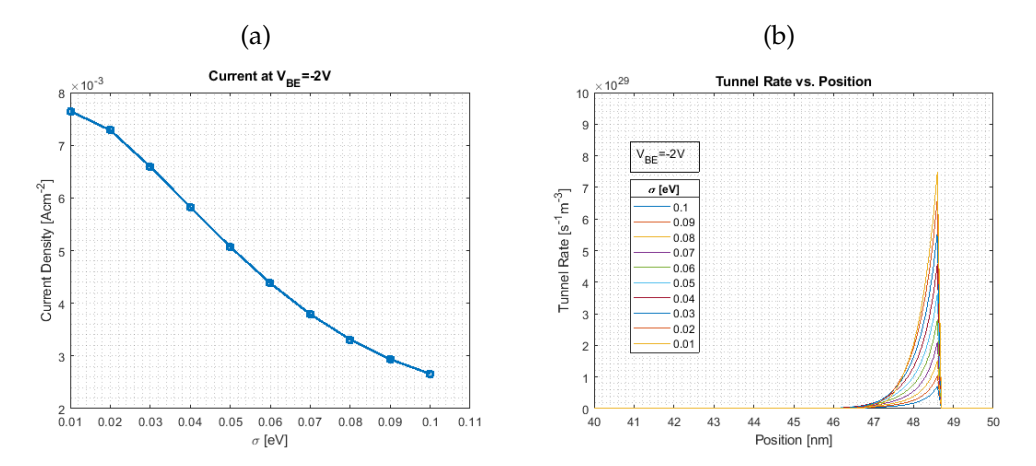


Figure S2: Dependence of the tunnel current in the device discussed in Figure S1 on the width of the density of states σ . The current decreases for a higher disorder, i.e. a larger σ (a), which is correlated to a higher tunnel rate for lower σ . The reduction in tunnel rate for larger σ can be explained by more states close the the transport level inside the organic semiconductor.

tunneling at lower energies due to a higher density of states tailing deeper into the HOMO/LUMO gap. Again, this results re-iterates the necessity that the energy dependence of the tunneling probability has to be taken into account in order to qualitatively treat charge injection into organic semiconductors.

3. Influence of Cathode Thickness on Diode Characteristic

In the main manuscript, the thickness of the cathode was varied from 13 nm to 19 nm, as the cathode will operate as base electrode in the final OPBT stack. However, as seen in Figure S₃, the thickness of the cathode has no influence on the device characteristics.

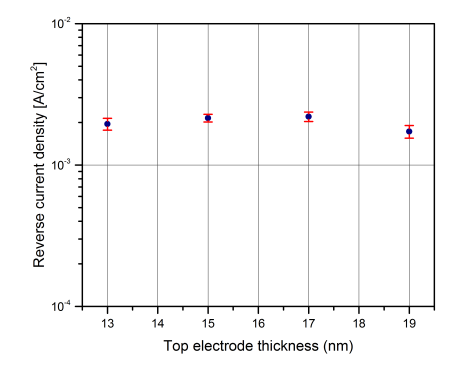


Figure S₃: Reverse current of diodes at a voltage of V=-4V. The thickness of the top electrode has no influence on the magnitude of the current.

4. Space Charge Limited Currents in Forward Direction

As discussed in the main manuscript, the current in forward direction scales with the inverse cube of the thickness of the C_{60} layer (cf. Figure 11). In Figure S4 it is shown that the current in forward direction scales with the square of the voltage as well, indicative of space charge limited currents.

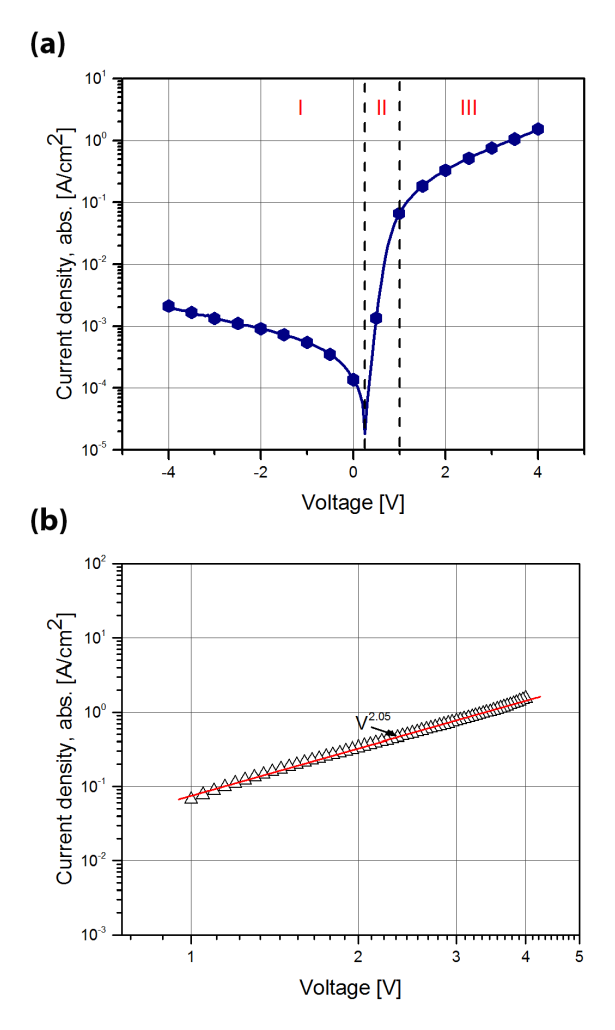


Figure S4: IV characteristic of organic diode discussed in the main text showing a V^2 dependency of its current. Combined with the cube dependency on the C_{60} layer thickness shown in the main manuscript one can conclude that the current is limited by space charges.

5. Simulation Parameters

Figure		S1	S ₂
	$\Delta x[nm]$	0.1	0.1
Cr	$\Delta E_1[eV]$	0.02	0.02
C_{60}	$\sigma[10^{-2}eV]$	10	10/9/8/7/6/5/4/3/2/1
	$d_{C60}[nm]$	50	50
	$N_0[m^{-3}]$	10^{27}	50 10 ²⁷
	$\mu_n[10^{-4}cm^2/Vs]$	1.5	1.5
	ϵ	4	4
	$\Delta E_3[eV]$	0.4	0.4
Al	$\Gamma_0[eV^{-1}s^{-1}]$	3×10^{10}	3×10^{10}
	$\Delta_E[eV]$	0.02	0.02

Figure		7a	7b
Cr	$\Delta x[nm]$	0.1	0.1
	$\Delta E_1[eV]$	0.02	0.02
C_{60}	$\sigma[eV]$	0.1	0.1
	$d_{C60}[nm]$	50	50
	$N_0[m^{-3}]$	10^{27}	10^{27}
	$\mu_n[10^{-4}cm^2/Vs]$	7.5	7.5
	ϵ_r	4	4
	$\Delta E_2[eV]$	0.8	0.8
Al_2O_3	ϵ_r	8	8
	$d_{ox}[nm]$	1	1/1.2/1.4/1.6/1.8
	$\Delta E_3[eV]$	1.15	1.15
Al	$\Gamma_0[eV^{-1}s^{-1}]$	3×10^{15}	3×10^{15}
	$\Delta_E[10^{-3}eV]$	5	5

Figure		7c	7e
Cr	$\Delta x[nm]$	0.1	0.1
	$\Delta E_1[eV]$	0.02	0.02
C_{60}	$\sigma[eV]$	0.1	0.1
	$d_{C60}[nm]$	50	50 10 ²⁷
	$N_0[m^{-3}]$	50 10 ²⁷	10^{27}
	$\mu_n[10^{-4}cm^2/Vs]$	1.5	3/6/7.5/12/24
	ϵ_r	4	4
	$\Delta E_2[eV]$	0.8	0.8
Al_2O_3	ϵ_r	8	8
	$d_{ox}[nm]$	1	1
	$\Delta E_{inj}[eV]$	1.17/1.15/1.13/1.11/1.09	1.15
Al	$\Gamma_0[eV^{-1}s^{-1}]$	3×10^{15}	3×10^{15}
	$\Delta_E[10^{-3}eV]$	5	5

Figure		8
Cr	$\Delta x[nm]$	0.1
	$\Delta E_1[eV]$	0.02
C_{60}	$\sigma[eV]$	0.1
	$d_{C60}[nm]$	20/25/50/100/150
	$N_0[m^{-3}]$	10^{27}
	$\mu_n[10^{-4}cm^2/Vs]$	7.5
	ϵ_r	4
	$\Delta E_2[eV]$	0.8
Al_2O_3	ϵ_r	8
	$d_{ox}[nm]$	1/ 1.2
	$\Delta E_3[eV]$	1.15
Al	$\Gamma_0[eV^{-1}s^{-1}]$	3×10^{15}
	$\Delta_E[10^{-3}eV]$	5

Figure		9a (symbol)	9a (red line)	9a (pink line)
Cr	$\Delta x[nm]$	0.1	0.1	0.1
	$\Delta t[ns]$	100	N.A.	N.A.
	$\Delta E_1[eV]$	0.02	0.02	0.02
C_{60}	$\sigma[eV]$	0.1	0.1	0.1
	$d_{C60}[nm]$	50	50	48
	$N_0[m^{-3}]$	10^{27}	10^{27}	10^{27}
	$\mu_n[10^{-4}cm^2/Vs]$	7.5	7.5	<i>7</i> ⋅5
	ϵ_r	4	4	4
C_{60}	$\sigma[eV]$	N.A.	N.A.	0.1
(traps)	$d_{C60}[nm]$	О	О	2
	$N_0[m^{-3}]$	N.A.	N.A.	10^{27}
	$\mu_n[10^{-4}cm^2/Vs]$	N.A.	N.A.	<i>7</i> ⋅5
	ϵ_r	N.A.	N.A.	4
	$N_{traps}[10^{19}cm^{-3}]$	N.A.	N.A.	5
	$E_{act}[eV]$	N.A.	N.A.	0.45
	$\Delta E_2[eV]$	0.8	N.A.	N.A.
Al_2O_3	ϵ_r	8	N.A.	N.A.
	$d_{ox}[nm]$	1	О	О
	$\Delta E_3[eV]$	1.15	0.35	0.35
Al	$\Gamma_0[eV^{-1}s^{-1}]$	3×10^{15}	N.A.	N.A.
	$\Delta_E[10^{-3}eV]$	5	N.A.	N.A.

Figure		9b
Cr	$\Delta x[nm]$	0.1
	$\Delta E_1[eV]$	0.02
C_{60}	$\sigma[eV]$	0.1
	$d_{C60}[nm]$	50/100/150
	$N_0[m^{-3}]$	10^{27}
	$\mu_n[10^{-4}cm^2/Vs]$	2
	ϵ_r	4
	$\Delta E_3[eV]$	0.35
Al		

Figure		10
Cr	$\Delta x[nm]$	0.1
	$\Delta E_1[eV]$	0.02
C_{60}	$\sigma[eV]$	0.1
	$d_{C60}[nm]$	100
	$N_0[m^{-3}]$	10^{27}
	$\mu_n[10^{-4}cm^2/Vs]$	7.5
	ϵ_r	4
	$\Delta E_2[eV]$	0.8
Al_2O_3	ϵ_r	8
	$d_{ox}[nm]$	0.8/0.9/1/1.2/1.4/1.6/1.8
	$\Delta E_3[eV]$	1.15
Al	$\Gamma_0[eV^{-1}s^{-1}]$	3×10^{15}
	$\Delta_E[10^{-3}eV]$	5

Figure		13a
Cr	$\Delta x[nm]$	0.1
	$\Delta E_1[eV]$	0.02
C_{60}	$\sigma[eV]$	0.1
	$d_{C60}[nm]$	100
	$N_0[m^{-3}]$	10^{27}
	$\mu_n[10^{-4}cm^2/Vs]$	7.5
	ϵ_r	4
	$\Delta E_2[eV]$	0.8
Al_2O_3	ϵ_r	8
	$d_{ox}[nm]$	0.8/0.9/1/1.1/1.2
	$\Delta E_3[eV]$	1.15
Al	$\Gamma_0[eV^{-1}s^{-1}]$	3×10^{15}
	$\Delta_E[10^{-3}eV]$	5